

Origin of Electrochromism in High-Performing Nanocomposite Nickel Oxide

Feng Lin,^{†,‡} Dennis Nordlund,[§] Tsu-Chien Weng,[§] Dimosthenis Sokaras,[§] Kim M. Jones,[†] Rob B. Reed,^{||} Dane T. Gillaspie,[†] Douglas G. J. Weir,[⊥] Rob G. Moore,^{||} Anne C. Dillon,[†] Ryan M. Richards,^{‡,||} and Chaiwat Engtrakul^{*,†}

[†]National Renewable Energy Laboratory, Golden, Colorado 80401, United States

[‡]Materials Science Program, Colorado School of Mines, Golden, Colorado 80401, United States

^{||}Department of Chemistry and Geochemistry, Colorado School of Mines, Golden, Colorado 80401, United States

[§]Stanford Synchrotron Radiation Lightsource at SLAC National Accelerator Laboratory, Menlo Park, California 94025, United States

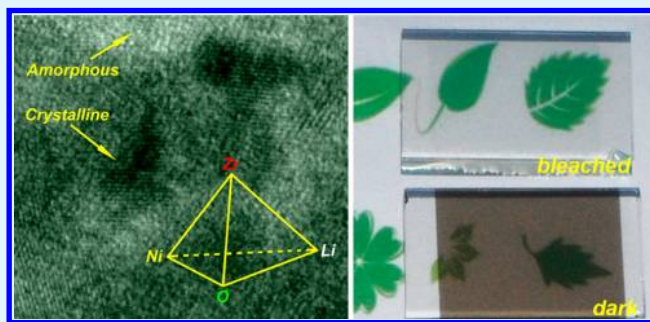
^{||}Stanford Institute for Materials & Energy Science at SLAC National Accelerator Laboratory, Menlo Park, California 94025, United States

[⊥]SAGE Electrochromics, Inc., Faribault, Minnesota 55021, United States

S Supporting Information

ABSTRACT: Electrochromic effects of transition metal oxides provide a great platform for studying lithium intercalation chemistry in solids. Herein, we report on an electronically modified nanocomposite nickel oxide (i.e., $\text{Li}_{2.34}\text{NiZr}_{0.28}\text{O}_x$) that exhibits significantly improved electrochromic performance relative to the state-of-the-art inorganic electrochromic metal oxides in terms of charge/discharge kinetics, bleached-state transparency, and optical modulation. The knowledge obtained from O K-edge X-ray absorption spectroscopy (XAS) and X-ray photoelectron spectroscopy (XPS) suggests that the internally grown lithium peroxide (i.e., Li_2O_2) species plays a major role in facilitating charge transfer thus enabling optimal electrochromic performance. This understanding is relevant to recent theoretical studies concerning conductivity in Li_2O_2 for lithium–air batteries (as cited in the main text). Furthermore, we elucidate the electrochromism in modified nickel oxide in lithium ion electrolyte with the aid of Ni K-edge XAS and Ni L-edge XAS studies. The electrochromism in the nickel oxide materials arises from the reversible formation of hole states on the NiO_6 units, which then impacts the Ni oxidation state through the $\text{Ni}3d\text{--O}2p$ hybridization states. This study sheds light on the lithium intercalation chemistry for general energy storage and semiconductor applications.

KEYWORDS: electrochromism, multicomponent, nickel oxide, X-ray absorption spectroscopy, lithium intercalation



1. INTRODUCTION

Unraveling the chemistry of lithium intercalation solids opens up new possibilities for discovering the next generation of rechargeable batteries,^{1,2} doping chemistry in semiconductors,³ and switchable glazing technologies (e.g., electrochromic windows).^{4–6} Electrochromic windows change light transmittance or reflectance properties in response to voltage (through reversible lithium intercalation) allowing for control of heat transfer and lighting conditions. This offers a paradigm for improving energy efficiency and daily comfort in buildings.⁷ A typical inorganic metal oxide-based electrochromic device consists of multiple layers where an ion conductor layer enables ions (e.g., lithium) to be shuttled between the cathodic and anodic electrode layers.⁸ The state-of-the-art anodic electrode materials are composed of complex mixtures of metal oxides predominately based on nickel oxide.^{9–13} In spite of significant

attempts to improve the function of anodic nickel oxide materials, these materials continue to exhibit relatively lackluster performance, such as inferior color contrast,¹⁴ poor bleached state transparency,¹⁵ slow switching kinetics,^{10,14,16,17} and limited durability.^{18,19} Unlike the clear electrochromism in conjugated polymers, the electrochromic mechanism (i.e., coloration process) in inorganic metal oxides, especially the anodic electrode layer, is not fully understood but is assumed to be related to the reversible $\text{Ni}^{2+}/\text{Ni}^{3+}$ redox process.²⁰ Elucidation of the electrochromic mechanism at the atomic level in nickel oxide must be achieved in order to synthesize new nickel oxide materials with the properties and behaviors

Received: January 9, 2013

Accepted: April 2, 2013

Published: April 2, 2013



necessary for broad implementation of this technology. Furthermore, we envision that an understanding of the lithium intercalation chemistry in electrochromic nickel oxide materials can have a significant impact on advancing similar energy efficient technologies, including batteries, semiconductors, and chemical catalysis. The formation of Li compounds (e.g., Li_2O_2) that facilitate more efficient Li^+/e^- intercalation processes has the potential to enable fast charge/discharge rates.^{21–23} Herein, we report a one-step cosputtering deposition method to synthesize nickel oxide-based anodic electrochromic materials containing multiple additives (e.g., Li and Zr) that facilitate fundamental studies regarding electrochromism in transition metal oxides.

2. EXPERIMENTAL METHODS

2.1. Materials Preparation. Radio frequency (RF) magnetron sputtering was performed on an Angstrom EvoVac deposition system housed in a glovebox under an argon atmosphere following a previously described method.¹³ Briefly, three-inch diameter metal alloy targets, Ni–Zr (80–20 at.%) and Ni–W (80–20 at.%), were purchased from ACI Alloys, while a three-inch diameter ceramic Li_2O target (99.9%) supported on a molybdenum backing plate was purchased from Plasmaterials, Inc. The gun powers for the metal alloy targets and ceramic target were 60 and 45 W, respectively. The target-substrate distance was 10 cm and remained constant throughout the study, and no additional heating was applied to the substrate. The base pressure and total deposition pressure were 10^{-7} Torr and 2 mTorr, respectively. The Ar/O_2 gas mixture was fixed at 1/2 throughout the study. The fluorine-doped tin oxide (FTO) glass substrates were purchased from Hartford Glass Co., Inc. ($\text{TEC } 15, 1.5'' \times 0.82'' \times 2.3$ mm). The substrates were cleaned successively with soapy water, deionized water, acetone, isopropyl alcohol, and dried under flowing N_2 . The materials fabricated from the cosputtering process were determined to be $\text{Li}_{2.34}\text{NiZr}_{0.28}\text{O}_x$ and $\text{Li}_{1.81}\text{NiW}_{0.21}\text{O}_x$ by ICP-MS (Tables S1 and S2). Using a similar protocol using pure Ni metal target but without Li_2O sputtering, we prepared NiO_x materials for control experiments. Ozone exposure of NiO_x electrode was performed following the procedure in a previously published work.²⁴

2.2. Materials Characterization. The crystal structures of the resulting films were characterized on a Philips X-ray diffractometer Model PW1729 operated at 45 kV and 40 mA using CuK_α radiation. Transmittance and reflectance measurements were performed on a Cary 6000i UV–vis–NIR spectrometer. Field emission scanning electron microscopy (FESEM) was done on a JEOL JSM-7000F Field Emission Scanning Electron Microscope with an EDAX Genesis EDS. X-ray photoelectron spectroscopy (XPS) was performed on a Kratos Axis HSi Ultra X-ray Photoelectron Spectrometer using an Al K_α X-ray source operated at 14 kV and 10 mA. The samples were prepared for transmission electron microscopy (TEM) using a NanoLab 200 Dual Beam FIB and analyzed on a FEI G²-T30 TEM operating at 300 kV. The ICP-MS used is a Perkin-Elmer NexION 300q with an S10 autosampler. Calibration standards for Li, Ni, W, and Zr were made using SPEX Certiprep ICP-MS standard solutions in 2% HCl (Optima trace metal grade). Dilutions of thin film digest solutions were made in 2% HCl. All dilutions were made in 15 mL Falcon polypropylene centrifuge tubes and analyzed immediately. Ex-situ soft X-ray XAS measurements were performed on the 31-pole wiggler beamline 10-1 at Stanford Synchrotron Radiation Lightsource (SSRL) using a ring current of 350 mA and a $1000 \text{ l}\cdot\text{mm}^{-1}$ spherical grating monochromator with $20 \mu\text{m}$ entrance and exit slits, providing $\sim 10^{11} \text{ ph}\cdot\text{s}^{-1}$ at 0.2 eV resolution in a 1 mm^2 beam spot. During the measurements, all samples were attached to an aluminum sample holder, and the surface was connected to the isolated holder using conductive carbon. Data were acquired in a single load at room temperature and under ultrahigh vacuum (10^{-9} Torr). Detection was performed in total electron yield (TEY) mode, where the sample drain current was normalized by the current from of a reference sample in a form of freshly evaporated gold on a thin grid positioned upstream of

the sample chamber. The penetration of TEY is $\sim 5 \text{ nm}$. Hard X-ray absorption data were collected at SSRL on beamline 6–2 experimental station 2 using a Si(311) double-crystal monochromator with a Rh-coated parabolic focusing mirror. X-ray energy was calibrated by collecting X-ray absorption of Ni foil with the first inflection point assigned as 8333 eV. The photon flux at 8.4 keV was $2 \times 10^{12} \text{ ph/s}$, and the beam size on the sample was $0.15 \text{ mm (V)} \times 0.4 \text{ mm (H)}$. A 1-m spherically bent analyzer crystal Si (551) was used to resolve Nickel K_β fluorescence line from scatterings and record High Energy Resolution Fluorescence Detection X-ray Absorption Spectroscopy (HERFD-XAS). The penetration depths of hard X-ray beam at 8264 and 8350 eV are 41 and $6 \mu\text{m}$, respectively. Since the X-rays penetrate through the film, no self-absorption effects due to the deep probing of fluorescence ($25 \mu\text{m}$) are expected. The samples were mounted on an aluminum stick, similar to the soft X-ray measurements.

2.3. Performance Evaluation. Electrochromic properties were measured in a liquid electrolyte half-cell where the electrolyte (Novolyte Technologies, part of the BASF Group) was 1 M lithium perchlorate (LiClO_4) dissolved in propylene carbonate (PC). Cyclic voltammetry (CV) was carried out using a BioLogic VMP3 multichannel potentiostat with a scan rate of 20 mV/s and a voltage range of 1.7–4.2 V vs Li/Li^+ . In-situ transmittance was measured using a diode laser at 670 nm. Switching kinetics (i.e., coloration and bleaching) were measured under potential step cycling from 1.7 to 4.2 V vs Li/Li^+ , where each potential step was maintained for 2 min. The switching speed is defined as the time required to achieve $\sim 90\%$ of total transmittance change within a potential step. All electrochemical measurements were carried out under an argon atmosphere in a glovebox. The samples were transferred from the sputtering chamber to testing cells without exposure to air or moisture.

3. RESULTS AND DISCUSSION

Structural characterization results for the as-deposited $\text{Li}_{2.34}\text{NiZr}_{0.28}\text{O}_x$ films prepared by RF magnetron sputtering are shown in Figure 1. Cross-sectional scanning electron microscopy (SEM) image (Figure 1a) shows a film thickness of ca. 80 nm, significantly thinner than most reported nickel oxide-based anodic electrodes.⁹ Figure 1b provides the X-ray

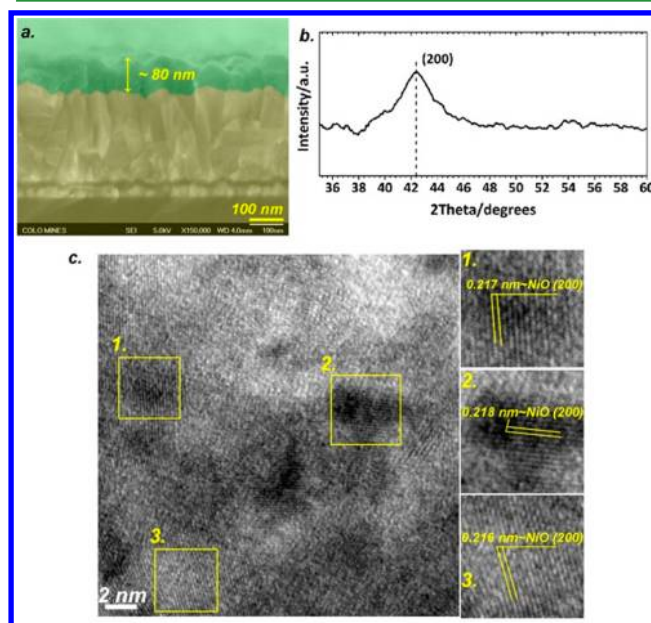


Figure 1. $\text{Li}_{2.34}\text{NiZr}_{0.28}\text{O}_x$ films prepared on fluorine-doped tin oxide: (a) cross-sectional SEM image, where the film is colored to enhance visualization, (b) smoothed XRD pattern, and (c) HRTEM image, where the selected crystallites are magnified for the determination of lattice spacing.

diffraction (XRD) pattern for the as-deposited $\text{Li}_{2.34}\text{NiZr}_{0.28}\text{O}_x$ film. The single peak at (200) indicates that nickel oxide nanocrystallites are preferentially oriented along $\langle 100 \rangle$ direction. Moreover, the diffraction angle ($2\theta = 42.5^\circ$) is shifted toward a lower value relative to the face center cubic NiO (JCPDS 65-2901)²⁵ indicating that the lattice constant of the nickel oxide-based material is expanded due to the presence of Zr and Li in the lattice, similarly to that observed in Nb-doped TiO_2 .⁴ A high-resolution transmission electron microscopy (HRTEM) image is shown in Figure 1c, where selected crystallites are magnified for the determination of lattice distances. Nickel oxide nanocrystallites are imbedded in an amorphous matrix, which is similar to the morphology observed in $\text{Li}_{1.2}\text{NiW}_{0.1}\text{O}_x$ ⁹ and Li-containing NiO .¹¹ These types of nanocomposite electrode materials have been shown to provide fast pathways for Li^+ diffusion.^{9,10} We note that the lattice distances of 0.216 nm, 0.217 nm, and 0.218 nm are slightly larger than the standard d_{200} (0.209 nm) of cubic NiO, which is consistent with the shift observed in the XRD pattern. Inductively coupled plasma mass spectroscopy (ICP-MS) analysis confirms that the molar ratio between Li and Ni is 2.34 (Table S1).

X-ray absorption spectroscopy (XAS) was employed to investigate the Li and Zr effects on the electronic structure of nickel oxide. Figure 2 presents a comparison of the Ni L-edge

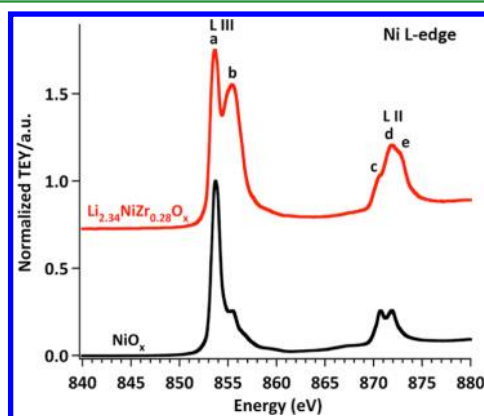


Figure 2. XAS spectra of Ni $\text{L}_{\text{II,III}}$ -edge in the total electron yield (TEY) mode, where the spectra have been normalized to the most intense peaks and overlapped along the Y-axis.

XAS for two nickel oxide-based thin films, corresponding to dipole transitions from Ni 2p to Ni 3d states, including both the $2p_{3/2}$ (L_{III}) and $2p_{1/2}$ (L_{II}) spin-orbit final states. Due to the direct dipole transition from 2p to 3d orbitals and the high resolution in the soft X-ray regime, L-edge XAS of the 3d transition metals is sensitive not only to the valency of the metal but also to the detailed energetics of the ligand-3d interactions governed in particular by symmetry as well as spin conservation and orbital hybridization.²⁶ Although rigorous treatment of all possible final states can be complicated,²⁷ the most salient features of the transition metal L-edge can be captured by atomic calculations with the introduction of crystal field effects.²⁶ We note that the XAS spectrum for a NiO_x film produced through RF magnetron sputtering closely resembles previously reported data for nickel oxide films.^{28,29} Here, the NiO_x XAS spectrum represents transitions from Ni ($2p^63d^8$) to Ni ($2p^53d^9$), where the final state as probed by XAS is well described by atomic multiplet calculations for a single Ni^{2+} in an octahedral coordination (Figure 2). Upon the addition of Li and Zr, the high-energy L_{III} feature **b** (and **e** for the L_{II} -edge) is

significantly enhanced. This is consistent with a formal increase in the oxidation state of nickel.^{28,29} A similar enhancement in the intensities of features **b** and **e** is observed for a NiO_x film after ozone exposure (Figure 3) previously found to increase

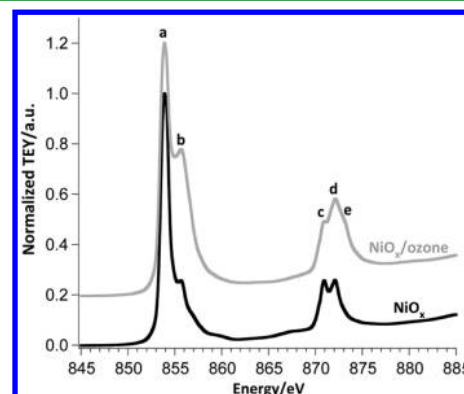


Figure 3. XAS spectra of Ni $\text{L}_{\text{II,III}}$ -edge of NiO_x materials in the total electron yield (TEY) mode, where the spectra have been normalized to the most intense peaks and overlapped along the Y-axis.

the amount of higher oxidation state nickel species.³⁰ We conclude that Li and Zr have been successfully doped into the nickel oxide lattice and modified its electronic structure. A nickel oxide-based electrode containing Li/W additives was prepared utilizing identical sputter deposition conditions as used for $\text{Li}_{2.34}\text{NiZr}_{0.28}\text{O}_x$. A chemical formula of $\text{Li}_{1.81}\text{NiW}_{0.21}\text{O}_x$ was determined by ICP-MS (Table S2). We note that the film thickness and crystal structure of the $\text{Li}_{1.81}\text{NiW}_{0.21}\text{O}_x$ film are identical to the $\text{Li}_{2.34}\text{NiZr}_{0.28}\text{O}_x$ film (Figure S1). The XAS spectrum for as-deposited $\text{Li}_{1.81}\text{NiW}_{0.21}\text{O}_x$ demonstrates a similar effect as observed in $\text{Li}_{2.34}\text{NiZr}_{0.28}\text{O}_x$ (Figure S2).

Cyclic voltammetry and in situ transmittance curves for $\text{Li}_{2.34}\text{NiZr}_{0.28}\text{O}_x$ and $\text{Li}_{1.81}\text{NiW}_{0.21}\text{O}_x$ thin film electrodes cycled in a 1 M LiClO_4 dissolved in propylene carbonate are displayed in Figures 4a and b. The charge capacities (as determined from the CVs for 80-nm-thick films) are 21.8 mC/cm^2 and 21.4 mC/cm^2 for the $\text{Li}_{2.34}\text{NiZr}_{0.28}\text{O}_x$ and $\text{Li}_{1.81}\text{NiW}_{0.21}\text{O}_x$ electrodes,

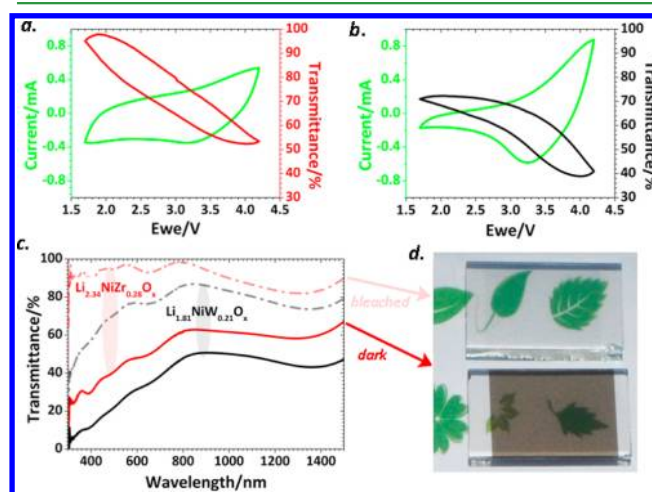


Figure 4. Cyclic voltammetry and in situ transmittance results (3rd cycle) of (a) $\text{Li}_{2.34}\text{NiZr}_{0.28}\text{O}_x$ and (b) $\text{Li}_{1.81}\text{NiW}_{0.21}\text{O}_x$ thin film electrodes, (c) ex-situ UV-vis-NIR spectra of bleached state (dash-dot) and dark state (solid) films, and (d) images of a $\text{Li}_{2.34}\text{NiZr}_{0.28}\text{O}_x$ film in the bleached (top) and dark (bottom) states.

respectively. Interestingly, these capacities are close to what Granqvist and co-workers proposed for practical device operation.³¹ The charge capacities for $\text{Li}_{2.34}\text{NiZr}_{0.28}\text{O}_x$ and $\text{Li}_{1.81}\text{NiW}_{0.21}\text{O}_x$ can be controlled (modified) easily by varying the film thickness. The optical modulation, measured as the transmittance difference between bleached and dark states, evaluates the dynamic range that an electrochromic film can achieve. The in situ optical modulation at 670 nm for the $\text{Li}_{2.34}\text{NiZr}_{0.28}\text{O}_x$ film is $\sim 45\%$ compared to $\sim 35\%$ for the $\text{Li}_{1.81}\text{NiW}_{0.21}\text{O}_x$ film. As determined by eq 1, where $\%T_b$ and $\%T_c$ represent the transmittances for bleached and dark states, respectively, the high specific optical density (defined as the optical density per micrometer) for the $\text{Li}_{2.34}\text{NiZr}_{0.28}\text{O}_x$ film ($11.7 \mu\text{m}^{-1}$ at 450 nm) is enhanced relative to the state-of-the-art porous WO_3 film ($9.0 \mu\text{m}^{-1}$ at 670 nm).³² A high specific optical density enables a reduction in film thickness without compromising optical contrast properties, therefore reducing manufacturing costs. It should be noted that a thicker $\text{Li}_{2.34}\text{NiZr}_{0.28}\text{O}_x$ film (~ 200 nm) shows significantly improved optical modulation ($\sim 75\%$ at 670 nm) while maintaining an optimal bleached state transparency (Figure 5). To the best of

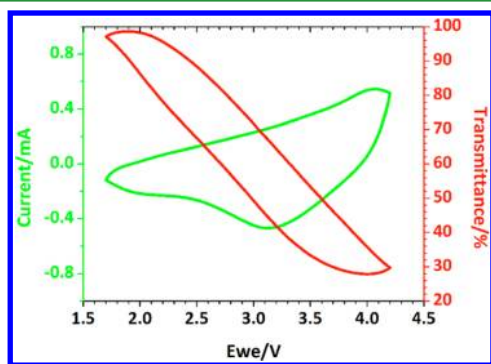


Figure 5. Cyclic voltammetry and in situ transmittance results (100th cycle) of a 200-nm-thick $\text{Li}_{2.34}\text{NiZr}_{0.28}\text{O}_x$ thin film electrode cycled in a 1 M LiClO_4 dissolved in propylene carbonate with a scan rate of 20 mV/s.

our knowledge, this optical modulation is the best performance for nickel oxide-based electrochromic materials in a lithium ion electrolyte. The coloration efficiencies of $\text{Li}_{2.34}\text{NiZr}_{0.28}\text{O}_x$ and $\text{Li}_{1.81}\text{NiW}_{0.21}\text{O}_x$ at 670 nm are *ca.* $33 \text{ cm}^2/\text{C}$ and *ca.* $31 \text{ cm}^2/\text{C}$, respectively. Importantly, the bleached state of $\text{Li}_{2.34}\text{NiZr}_{0.28}\text{O}_x$ film is much more transparent than that of $\text{Li}_{1.81}\text{NiW}_{0.21}\text{O}_x$ film. Figure 4c provides the UV–vis–NIR spectra (300–1500 nm) for bleached and dark films. The transmittance of nickel oxide films typically decreases when the irradiation wavelength is less than 800 nm.⁹ However, the decrease does not occur in the bleached state of the $\text{Li}_{2.34}\text{NiZr}_{0.28}\text{O}_x$ film. A significantly larger contrast in the bleached state transparency is observed for the $\text{Li}_{2.34}\text{NiZr}_{0.28}\text{O}_x$ film in the UV–vis region relative to the $\text{Li}_{1.81}\text{NiW}_{0.21}\text{O}_x$ film.

$$\text{Specific optical density} = \ln(\%T_b/\%T_c)/\text{thickness} \quad (1)$$

A relative determination of perceived light intensity with respect to the human eye is necessary when a high level of transparency and near colorlessness is desired in the bleached state of an electrochromic device. Therefore, utilizing the UV–vis–NIR data in Figure 4c, the CIE-defined $L^*a^*b^*$ color coordinates³³ are calculated as detailed in the Supporting Information. The b^* values for the bleached states of

$\text{Li}_{2.34}\text{NiZr}_{0.28}\text{O}_x$ and $\text{Li}_{1.81}\text{NiW}_{0.21}\text{O}_x$ are estimated to be 6.5 and 12.6, respectively. A b^* value below 8 is typically undetectable by the human eye indicating that the bleached state for $\text{Li}_{2.34}\text{NiZr}_{0.28}\text{O}_x$ is nearly colorless (no remnant yellow color, Figure 4d). This improved transparency across the spectrum allows for more efficient control of solar heat gain and natural light harnessing.

Electrochromic processes in nickel oxide anodic electrodes are typically slower than in cathodic WO_3 electrodes and impede the overall switching kinetics of a layered electrochromic device.^{10,14,16} Wet-chemical synthesis routes have been employed to fabricate porous nickel oxide structures in order to reduce the switching time from one state to another state.^{14,34} Improved optical switching (insertion and removal of lithium) has also been observed in modified nickel oxide films synthesized using conventional sputter techniques.³⁵ The normalized in situ transmittance changes under potential step cycling are shown in Figures S3a and b, for $\text{Li}_{2.34}\text{NiZr}_{0.28}\text{O}_x$ and $\text{Li}_{1.81}\text{NiW}_{0.21}\text{O}_x$, respectively. The switching speed is defined as the time required to achieve $\sim 90\%$ of transmittance change upon a potential step. In Li-ion electrolyte, the bleaching and coloration kinetics are both greatly improved for the $\text{Li}_{2.34}\text{NiZr}_{0.28}\text{O}_x$ film, with bleaching (T_b) and coloration (T_c) times of 18 and 20 s, respectively. The T_b and T_c times for $\text{Li}_{1.81}\text{NiW}_{0.21}\text{O}_x$ are 61 and 31 s, respectively. The switching kinetics of the $\text{Li}_{2.34}\text{NiZr}_{0.28}\text{O}_x$ is equivalent with the state-of-the-art WO_3 materials^{32,36} and much improved relative to the reported nickel oxide-based electrode.¹⁶

The interface between an electrochromic film and electrolyte plays a crucial role in facilitating the efficient insertion and removal of lithium. The surface composition of the nickel oxide-based electrodes was probed with X-ray photoelectron spectroscopy (XPS) and O K-edge XAS. As shown in Figure S4, the XPS spectra for $\text{Li}_{2.34}\text{NiZr}_{0.28}\text{O}_x$ and $\text{Li}_{1.81}\text{NiW}_{0.21}\text{O}_x$ clearly demonstrate that the surface composition of the modified nickel-oxide films depends on the metal additives (Li/Zr vs Li/W). High-resolution XPS identified every element (i.e., Li, Ni, W, and O) present in the $\text{Li}_{1.81}\text{NiW}_{0.21}\text{O}_x$ film. However, only Li and O are observed for the $\text{Li}_{2.34}\text{NiZr}_{0.28}\text{O}_x$ film. This observation suggests that phase separation occurs during the deposition of the $\text{Li}_{2.34}\text{NiZr}_{0.28}\text{O}_x$ film, and a lithium-rich layer (Li_2O and/or Li_2O_2) is generated on the surface of the film. Oxygen K-edge XAS probes the local unoccupied states with p character (via the dipole transition from O 1s), which in transition metal (TM) oxides are sensitive to the exact nature of the O2p–TM3d hybridization as dictated by symmetry.^{26,37} As reported by Kuiper et al., O K-edge XAS from NiO_x films is expected to display a strong sensitivity to doping.³⁸ Figure 6 shows O K-edge XAS spectra for NiO_x , $\text{Li}_{1.81}\text{NiW}_{0.21}\text{O}_x$, and $\text{Li}_{2.34}\text{NiZr}_{0.28}\text{O}_x$ materials. The pre-edge feature at *ca.* 527 eV is attributed to the extra holes introduced by the doping. Oxygen K-edge XAS can also provide more information on the lithium-rich layer due to its sensitivity to ionicity and local structure of O ions in lithium compounds.^{39,40} For the $\text{Li}_{2.34}\text{NiZr}_{0.28}\text{O}_x$ film we observe a remarkably different spectrum with a strong resonance at *ca.* 531 eV, which can be attributed to the O 1s $\rightarrow \pi^*$ transition of lithium peroxide (i.e., Li_2O_2).³⁹ Note that a few nanometer thick Li_2O_2 layer is needed to suppress the nickel oxide related features. For the $\text{Li}_{1.81}\text{NiW}_{0.21}\text{O}_x$ film, this Li_2O_2 peak intensity is significantly reduced (only a very small O 1s $\rightarrow \pi^*$ peak is observed), consistent with XPS (Figure S4) and the absence of a lithium-dominated surface layer. To the best of our

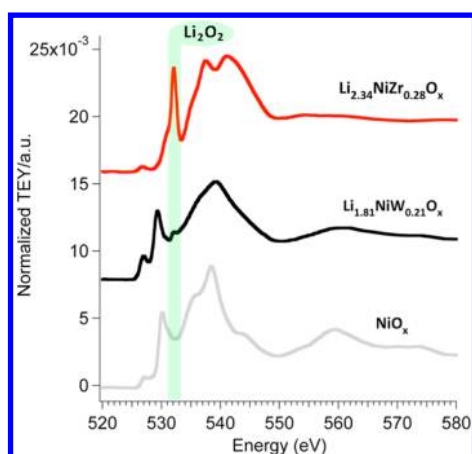


Figure 6. (a) Oxygen K-edge XAS spectra for NiO_x , $\text{Li}_{1.81}\text{NiW}_{0.21}\text{O}_x$, and $\text{Li}_{2.34}\text{NiZr}_{0.28}\text{O}_x$ films.

knowledge, this is the first time that Li_2O_2 has been integrated into an electrochromic electrode. Recent theoretical studies showed that Li_2O_2 could be beneficial for Li^+/e^- diffusion.^{21–23} Our present study suggests that the formation of a surface Li_2O_2 layer facilitates the efficient diffusion of Li^+/e^- and accounts for the superior switching kinetics observed in $\text{Li}_{2.34}\text{NiZr}_{0.28}\text{O}_x$ relative to $\text{Li}_{1.81}\text{NiW}_{0.21}\text{O}_x$.

The electrochromic mechanism of nickel oxide-based materials in Li-ion electrolytes can be elucidated by X-ray absorption spectroscopic studies. In Figure 7, a Ni K-edge and

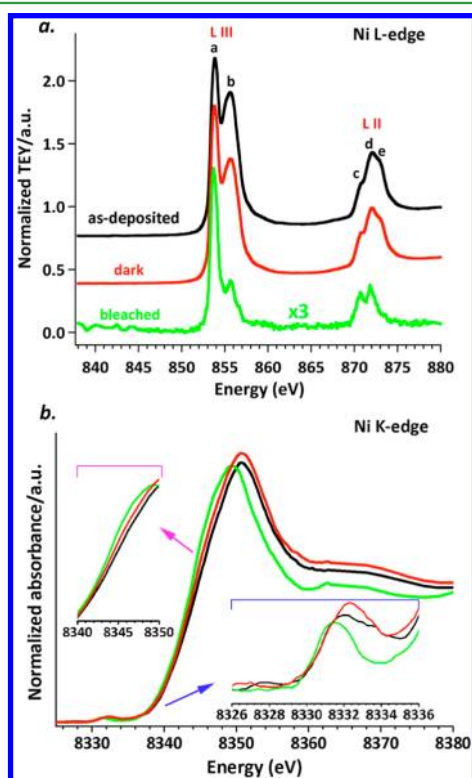


Figure 7. X-ray absorption spectra for the $\text{Li}_{2.34}\text{NiZr}_{0.28}\text{O}_x$ film: (a) Ni L-edge XAS of the as-deposited, bleached and dark states for $\text{Li}_{2.34}\text{NiZr}_{0.28}\text{O}_x$; (b) Ni K-edge XAS of the as-deposited (black), bleached (green) and dark (red) states for $\text{Li}_{2.34}\text{NiZr}_{0.28}\text{O}_x$, where the insets display the magnifications for the pre-edge feature and absorption edge.

Ni L-edge XAS study is provided to shed light on the electrochromism in $\text{Li}_{2.34}\text{NiZr}_{0.28}\text{O}_x$. As shown in Figure 7a, there is minimal difference between the Ni L-edge XAS spectra for the $\text{Li}_{2.34}\text{NiZr}_{0.28}\text{O}_x$ dark-state and as-deposited $\text{Li}_{2.34}\text{NiZr}_{0.28}\text{O}_x$ films. The spectra are consistent with the presence of high valence state Ni species (i.e., high hole concentration).²⁹ The location of the hole states is described below. The Ni L-edge XAS spectrum for the $\text{Li}_{2.34}\text{NiZr}_{0.28}\text{O}_x$ bleached state shows a significant decrease in the intensities of features b and e relative to the dark-state, indicating a loss of hole states (Figure 7a). We interpret these results as a neutralization of the initial hole states by electrons from the external circuit leading to the bleached nickel oxide film. The penetration depth of soft X-rays (i.e., Ni L-edge) is limited to ~ 5 nm. To probe the bulk electronic structure of nickel oxide in $\text{Li}_{2.34}\text{NiZr}_{0.28}\text{O}_x$ throughout the entire film, Ni K-edge XAS was measured (Figure 7b). Shifts in the pre-edge feature and absorption edge in the Ni K-edge XAS can be associated with the holes introduced by doping nickel oxide with lithium oxide, as reported by Pickering et al.⁴¹ The pre-edge feature and absorption edge both shift to higher energy as the $\text{Li}_{2.34}\text{NiZr}_{0.28}\text{O}_x$ film is cycled from the bleached state to the dark state indicating an increase in holes in the NiO_6 unit. The observed change in the nickel oxide electronic structure with cycling as observed with Ni K-edge XAS is consistent with the soft X-ray data in Figure 7a. These XAS data further confirm that the electrochromic process can be associated with a reversible change in the Ni oxidation state, which is closely related to the well-known Bode mechanism.⁴² An identical Ni K-edge and Ni L-edge XAS study on $\text{Li}_{1.81}\text{NiW}_{0.21}\text{O}_x$ confirms that this mechanism is applicable for various nickel oxide-based anodic electrodes in Li-ion electrolytes (Figure S2).

We note that although the XAS spectral changes (Figures 7 and S2) are consistent with a formal increase in the oxidation state of nickel, it has been shown that the Ni L-edge in Li-doped NiO cannot simply be ascribed by a linear combination of Ni^{2+} and Ni^{3+} in an octahedral environment using crystal field theory.²⁹ Sawatzky and co-workers interpreted the Ni L-edge XAS spectra for Li-doped NiO by accounting for the hybridization of the doped holes with the Ni 3d states and concluded that the doped holes must be delocalized over the oxygen sites on the NiO_6 cluster.²⁹ This interpretation is supported by previous O K-edge XAS³⁸ and subsequent *ab initio* calculations.⁴³ However, a recent density functional calculation on Li-doped NiO using both the HSE06 hybrid functional and density functional theory + *U* approaches showed that the system is better described with the hole localized on the nickel ion.⁴⁴ Although the exact nature of the hole states in lithium-doped nickel oxides remains a topic of intense study, the presence of holes and the sensitivity of XAS to the changes in the electronic structure of nickel oxide is well supported. It should also be noted that lithium intercalation during material preparation (synthesis) or during electrochemical cycling imposes different effects on the electronic structure of the NiO_6 unit, which provides alternative opportunities for selectively synthesizing p-type or n-type doped semiconductors.

4. CONCLUSION

In conclusion, electronically modified multicomponent and high-performing nickel oxide-based electrochromic counter electrodes were fabricated *via* a novel one-step RF magnetron cosputtering technique. This deposition technique yields high-

quality nanocomposite electrochromic films and affords tunable control of material composition and structure that allowed us to pursue the fundamental mechanisms of electrochromism in nickel oxide. Specifically, the electrochromic effect in multi-component nickel oxide-based materials was found to arise from the reversible formation of hole states in the NiO_6 cluster. This mechanistic representation was supported by XAS and is consistent with a formal change of Ni oxidation states. Additionally, the incorporation of Li_2O_2 enhanced material performance and may explain the origin of differing charge and discharge rates of $\text{Li}_{2.34}\text{NiZr}_{0.28}\text{O}_x$ and $\text{Li}_{1.81}\text{NiW}_{0.21}\text{O}_x$. We anticipate that this understanding will provide further insight into the “doping” effects on metal oxide materials for electrochromic applications as well as other energy storage applications (e.g., lithium–air batteries).

■ ASSOCIATED CONTENT

■ Supporting Information

CIE b^* calculation method, ICP-MS tables, SEM and XRD for $\text{Li}_{1.81}\text{NiW}_{0.21}\text{O}_x$, ex-situ XAS spectra for $\text{Li}_{1.81}\text{NiW}_{0.21}\text{O}_x$, normalized switching kinetics and XPS spectra for as-deposited $\text{Li}_{2.34}\text{NiZr}_{0.28}\text{O}_x$ and $\text{Li}_{1.81}\text{NiW}_{0.21}\text{O}_x$. This material is available free of charge via the Internet at <http://pubs.acs.org>.

■ AUTHOR INFORMATION

Corresponding Author

*E-mail: chaiwat.engtrakul@nrel.gov.

Notes

The authors declare no competing financial interest.

■ ACKNOWLEDGMENTS

This paper is dedicated to the loving memory of Anne C. Dillon. This research was supported by the U.S. Department of Energy under Contract DE-AC36-08-GO28308 with the National Renewable Energy Laboratory as part of the DOE Office of Energy Efficiency and Renewable Energy Office of Building Technologies Program. Portions of this research were carried out at the Stanford Synchrotron Radiation Laboratory, a national user facility operated by Stanford University on behalf of the U.S. Department of Energy, Office of Basic Energy Sciences.

■ REFERENCES

- (1) Tarascon, J. M.; Armand, M. *Nature* **2001**, *414*, 359–367.
- (2) Bruce, P. G.; Scrosati, B.; Tarascon, J. M. *Angew. Chem., Int. Ed.* **2008**, *47*, 2930–2946.
- (3) Lee, J.; Cha, S.; Kim, J.; Nam, H.; Lee, S.; Ko, W.; Wang, K. L.; Park, J.; Hong, J. *Adv. Mater.* **2011**, *23*, 4183–4187.
- (4) Ghicov, A.; Yamamoto, M.; Schmuki, P. *Angew. Chem., Int. Ed.* **2008**, *47*, 7934–7937.
- (5) Chernova, N. A.; Roppolo, M.; Dillon, A. C.; Whittingham, M. S. *J. Mater. Chem.* **2009**, *19*, 2526–2552.
- (6) Nah, Y. C.; Ghicov, A.; Kim, D.; Berger, S.; Schmuki, P. *J. Am. Chem. Soc.* **2008**, *130*, 16154–16155.
- (7) Lee, E. S.; Claybaugh, E. S.; LaFrance, M. *Energy Build.* **2012**, *47*, 267–284.
- (8) Granqvist, C. R. *Nat. Mater.* **2006**, *5*, 89–90.
- (9) Gillaspie, D.; Norman, A.; Tracy, C. E.; Pitts, J. R.; Lee, S. H.; Dillon, A. *J. Electrochem. Soc.* **2010**, *157*, H328–H331.
- (10) Lee, S. H.; Joo, S. K. *Sol. Energy Mater. Sol. Cells* **1995**, *39*, 155–166.
- (11) Moulki, H.; Park, D. H.; Min, B.-K.; Kwon, H.; Hwang, S.-J.; Choy, J.-H.; Toupance, T.; Campet, G.; Rougier, A. *Electrochim. Acta* **2012**, *74*, 46–52.
- (12) Green, S. V.; Pehlivan, E.; Granqvist, C. G.; Niklasson, G. A. *Sol. Energy Mater. Sol. Cells* **2012**, *99*, 339–344.
- (13) Lin, F.; Nordlund, D.; Weng, T.-C.; Moore, R. G.; Gillaspie, D. T.; Dillon, A. C.; Richards, R. M.; Engtrakul, C. *ACS Appl. Mater. Interfaces* **2013**, *5*, 301–309.
- (14) Yuan, Y. F.; Xia, X. H.; Wu, J. B.; Chen, Y. B.; Yang, J. L.; Guo, S. Y. *Electrochim. Acta* **2011**, *56*, 1208–1212.
- (15) Avendano, E.; Azens, A.; Niklasson, G. A.; Granqvist, C. G. *Sol. Energy Mater. Sol. Cells* **2004**, *84*, 337–350.
- (16) Tenent, R. C.; Gillaspie, D. T.; Miedaner, A.; Parilla, P. A.; Curtis, C. J.; Dillon, A. C. *J. Electrochem. Soc.* **2010**, *157*, H318–H322.
- (17) Lin, F.; Gillaspie, D. T.; Dillon, A. C.; Richards, R. M.; Engtrakul, C. *Thin Solid Films* **2013**, *527*, 26–30.
- (18) Penin, N.; Rougier, A.; Laffont, L.; Poizot, P.; Tarascon, J. M. *Sol. Energy Mater. Sol. Cells* **2006**, *90*, 422–433.
- (19) Bouessaya, I.; Rougier, A.; Poizot, P.; Moscovici, J.; Michalowicz, A.; Tarascon, J. M. *Electrochim. Acta* **2005**, *50*, 3737–3745.
- (20) Gillaspie, D. T.; Tenent, R. C.; Dillon, A. C. *J. Mater. Chem.* **2010**, *20*, 9585–9592.
- (21) Hummelshøj, J. S.; Blomqvist, J.; Datta, S.; Vegge, T.; Rossmeisl, J.; Thygesen, K. S.; Luntz, A. C.; Jacobsen, K. W.; Nørskov, J. K. *J. Chem. Phys.* **2010**, *132*, 071101.
- (22) Radin, M. D.; Rodriguez, J. F.; Tian, F.; Siegel, D. J. *J. Am. Chem. Soc.* **2012**, *134*, 1093–1103.
- (23) Zhao, Y.; Ban, C.; Kang, J.; Santhanagopalan, S.; Kim, G.-H.; Wei, S.-H.; Dillon, A. C. *Appl. Phys. Lett.* **2012**, *101*, 023903.
- (24) Lin, F.; Li, C.-P.; Chen, G.; Tenent, R. C.; Wolden, C. A.; Gillaspie, D. T.; Dillon, A. C.; Richards, R. M.; Engtrakul, C. *Nanotechnology* **2012**, *23*, 255601.
- (25) Hu, J. C.; Zhu, K. K.; Chen, L. F.; Yang, H. J.; Li, Z.; Suchopar, A.; Richards, R. *Adv. Mater.* **2008**, *20*, 267–271.
- (26) Degroot, F. M. F.; Fuggle, J. C.; Thole, B. T.; Sawatzky, G. A. *Phys. Rev. B* **1990**, *42*, 5459–5468.
- (27) Wasinger, E. C.; de Groot, F. M. F.; Hedman, B.; Hodgson, K. O.; Solomon, E. I. *J. Am. Chem. Soc.* **2003**, *125*, 12894–12906.
- (28) Vanelp, J.; Searle, B. G.; Sawatzky, G. A.; Sacchi, M. *Solid State Commun.* **1991**, *80*, 67–71.
- (29) Vanveenendaal, M. A.; Sawatzky, G. A. *Phys. Rev. B* **1994**, *50*, 11326–11331.
- (30) Ratcliff, E. L.; Meyer, J.; Steirer, K. X.; Garcia, A.; Berry, J. J.; Ginley, D. S.; Olson, D. C.; Kahn, A.; Armstrong, N. R. *Chem. Mater.* **2011**, *23*, 4988–5000.
- (31) Azens, A.; Kullman, L.; Granqvist, C. G. *Sol. Energy Mater. Sol. Cells* **2003**, *76*, 147–153.
- (32) Lin, F.; Cheng, J.; Engtrakul, C.; Dillon, A. C.; Nordlund, D.; Moore, R. G.; Weng, T.-C.; Williams, S. K. R.; Richards, R. M. *J. Mater. Chem.* **2012**, *22*, 16817–16823.
- (33) *CIE Technical Report: Colorimetry*, 3rd ed; Commission Internationale De L'eclairage: Vienna, Austria, 2004.
- (34) Huang, H.; Tian, J.; Zhang, W. K.; Gan, Y. P.; Tao, X. Y.; Xia, X. H.; Tu, J. P. *Electrochim. Acta* **2011**, *56*, 4281–4286.
- (35) Lee, S. H.; Park, Y. S.; Joo, S. K. *Solid State Ionics* **1998**, *109*, 303–310.
- (36) Brezesinski, T.; Fattakhova-Rohlfing, D.; Sallard, S.; Antonietti, M.; Smarsly, B. M. *Small* **2006**, *2*, 1203–1211.
- (37) Abbate, M.; Degroot, F. M. F.; Fuggle, J. C.; Fujimori, A.; Tokura, Y.; Fujishima, Y.; Strebel, O.; Domke, M.; Kaindl, G.; Vanelp, J.; Thole, B. T.; Sawatzky, G. A.; Sacchi, M.; Tsuda, N. *Phys. Rev. B* **1991**, *44*, 5419–5422.
- (38) Kuiper, P.; Kruizinga, G.; Ghijsen, J.; Sawatzky, G. A.; Verweij, H. *Phys. Rev. Lett.* **1989**, *62*, 221–224.
- (39) Chan, M. K. Y.; Shirley, E. L.; Karan, N. K.; Balasubramanian, M.; Ren, Y.; Greeley, J. P.; Fister, T. T. *J. Phys. Chem. Lett.* **2011**, *2*, 2483–2486.
- (40) Ruckman, M. W.; Chen, J.; Qiu, S. L.; Kuiper, P.; Strongin, M. *Phys. Rev. Lett.* **1991**, *67*, 2533–2536.
- (41) Pickering, I. J.; George, G. N.; Lewandowski, J. T.; Jacobson, A. J. *J. Am. Chem. Soc.* **1993**, *115*, 4137–4144.

- (42) Niklasson, G. A.; Granqvist, C. G. *J. Mater. Chem.* **2007**, *17*, 127–156.
- (43) Mackrodt, W. C.; Harrison, N. M.; Saunders, V. R.; Allan, N. L.; Towler, M. D. *Chem. Phys. Lett.* **1996**, *250*, 66–70.
- (44) Chen, H. R.; Harding, J. H. *Phys. Rev. B* **2012**, *85*, 115127.